RSC Advances

PAPER

View Article Online
View Journal | View Issue

Cite this: *RSC Adv.*, 2019, **9**, 17165

Surfactant-assisted microwave processing of ZnO particles: a simple way for designing the surface-to-bulk defect ratio and improving photo(electro) catalytic properties

Smilja Marković, *[a] Ivana Stojković Simatović, [b] Sanita Ahmetović,[c] Ljiljana Veselinović, [a] Stevan Stojadinović, [d] Vladislav Rac,[e] Srečo Davor Škapin, [f] Danica Bajuk Bogdanović, [b] Ivona Janković Častvan[g] and Dragan Uskoković [a]

ZnO nanopowders were produced using microwave processing of a precipitate and applied as a photoanode for photoelectrochemical water splitting. Two different surfactants, cetyltrimethylammonium bromide (CTAB) as the cationic and Pluronic F127 as the non-ionic one, were employed to *in situ* adjust the surface-to-bulk defect ratio in the ZnO crystal structure and further to modify the photo(electro)catalytic activity of the ZnO photoanode. The crystal structure, morphological, textural, optical and photo(electro)catalytic properties of ZnO particles were studied in detail to explain the profound effects of the surfactants on the photoanode activity. The ZnO/CTAB photoanode displayed the highest photocurrent density of 27 mA g^{-1}, compared to ZnO (10.4 mA g^{-1}) and ZnO/F127 photoanodes (20 mA g^{-1}) at 1.5 V *vs.* SCE in 0.1 M Na_2SO_4 under visible illumination of 90 mW cm^{-2}. A significant shift of the overpotential toward lower values was also observed when photoanodes were illuminated. The highest shift of the overpotential, from 1.296 to 0.248 V *vs.* SCE, was recorded when the ZnO/CTAB photanode was illuminated. The ZnO/CTAB photoanode provides efficient charge transfer across the electrode/electrolyte interface, with a longer lifetime of photogenerated electron–hole pairs and reduced possibility of charge recombination. The photoconversion efficiency was improved from 1.4% for ZnO and 0.9% for ZnO/F127 to 4.2% for ZnO/CTAB at 0.510 mV. A simple procedure for the synthesis of ZnO particles with improved photo(electro)catalytic properties was established and it was found that even a small amount of CTAB used during processing of ZnO increases the surface-to-bulk defect ratio. Optimization of the surface-to-bulk defect ratio in ZnO materials enables increase of the absorption capacity for visible light, rendering of the recombination rate of the photogenerated pair, as well as increase of both the photocurrent density and photoconversion efficiency.

Received 4th April 2019
Accepted 21st May 2019

DOI: 10.1039/c9ra02553g

rsc.li/rsc-advances

1. Introduction

Since 1972 when Fujishima and Honda published the first paper on the photoelectrolysis of water using TiO_2 as a photoanode,[1] numerous efforts have been made by materials scientists to develop photocatalysts that would be more efficient under sunlight irradiation.[2–4] In the 21st century, when we are facing an energy crisis and environmental pollution as one of the major global problems, the idea developed by Fujishima and Honda is more popular than ever since solar-driven photoelectrochemical (PEC) water splitting of semiconductor catalysis can be used for efficient conversion of solar energy to chemical energy or electricity.[5–7] An efficient photoactive material should meet both kinetic and thermodynamic criteria for the photoconversion of solar energy to chemical energy or electricity.[7] In order to be suited for this purpose, photoactive materials need to: (1) absorb both ultraviolet and visible light irradiation producing electron–hole pairs, (2) separate electrons and holes in space to prevent their recombination, (3) provide rapid charge transfer across the electrode/electrolyte interface, (4) have suitable redox potentials to drive photo-oxidative reactions, (5) have a high photo-corrosion resistivity, and (6) to be recyclable, either for the sake of reuse or to prevent further water contamination.[3,7–12] Over the years, metal oxides such as

[a]*Institute of Technical Sciences of SASA, Knez Mihailova 35/IV, 11000 Belgrade, Serbia. E-mail: smilja.markovic@itn.sanu.ac.rs*
[b]*University of Belgrade, Faculty of Physical Chemistry, Belgrade, Serbia*
[c]*University of Belgrade, Institute for Multidisciplinary Research, Serbia*
[d]*University of Belgrade, Faculty of Physics, Belgrade, Serbia*
[e]*University of Belgrade, Faculty of Agriculture, Belgrade, Serbia*
[f]*Jožef Stefan Institute, Ljubljana, Slovenia*
[g]*University of Belgrade, Faculty of Technology and Metallurgy, Belgrade, Serbia*

TiO_2, ZnO, SnO_2, Fe_2O_3, CoO, V_2O_5, WO_3, *etc.*, have been studied as the photoanodes for solar-driven PEC water splitting due to their high photoactivity and photostability.[4,8,13–19] Noble metal nanocomposites, especially Ag-based,[20] as well as metal chalcogenides such as CuSe, CdS, MoS_2, Ag_2S, *etc.*, have also been studied as promising visible light photocatalysts and electrocatalysts due to their suitable band gap (<2.5 eV) and excellent absorption of visible light.[21–23] Newly developed sophisticated materials such as: metal–organic frameworks (MOFs), covalent–organic frameworks (COFs), zeolite–imidazole frameworks (ZIFs), porous coordination polymers (PCPs) have shown high photocatalytic or electrocatalytic activity.[24] Over the past few years, since the pioneering study in 2009 by Wang and coworkers,[25] semiconductor polymeric graphitic carbon nitride (g-C_3N_4) photocatalysts have attracted intensely growing interests in the research area of visible-light-induced hydrogen evolution reaction because of their facile synthesis, easy functionalization, attractive electronic band structure, high physicochemical stability and photocatalytic activity.[26]

Although their application as a photoanode under direct sunlight illumination is restricted by a wide band gap (>3 eV), allowing the absorption of UV light only, ZnO-based materials, together with TiO_2, are the most intensively investigated photo(electro)catalytic materials. ZnO is a significantly better conductor of both electrons and holes than many photocatalysts, even TiO_2,[8] and due to this it is worth trying to overcome the disadvantages of ZnO-based materials related to optical absorption and sunlight photonic activity. Different approaches have been developed for enhancing the optical properties of ZnO materials: incorporation of transition metal ions into the crystal structure, sensitization of particle surface, hydrogenation, incorporation of crystalline defects in metal oxide semiconductors in the form of vacancies and interstitials, *etc.*[9,27–30]

Crystalline defects can strongly influence electrical and optical properties of a semiconductor. Defects often introduce levels in the band gap of semiconductors;[31] these levels involve transitions between different charge states of the same defect. Surface defects can improve absorption capacity while bulk defects, commonly oxygen vacancies, can act as recombination centers leading to the loss of photocatalytic efficiency.[32] It has been reported that tuning the relative concentration ratio of surface to bulk defects in semiconductor nanocrystals can improve the separation of photogenerated electron–hole and therefore can enhance photocatalytic efficiency.[33] Accordingly, understanding the relationship between point defects, especially the surface-to-bulk defect ratio, and photo(electro)catalytic efficiency is important for successful application of ZnO as a photoanode materials.

In our previous work, we studied the influence of point defects on the crystal structure, optical and photocatalytic properties of microwave processed ZnO particles. To vary the concentration and the type of point defects, we used polyethylene oxide (PEO) with different molecular weights (200 000, 600 000 and 900 000 g mol^{-1}).[30] We demonstrated that oxygen interstitials at the surface of ZnO particles had profound effects on the direct sunlight photodegradation of methylene blue. The aim of this research is to *in situ* modify the surface-to-bulk defects ratio in ZnO particles by surfactant-directed microwave processing. Surfactants have so far been used mostly as an aid in hydrothermal, solvothermal or sol–gel processes, as they may help prepare monodisperse particles with narrow size distributions, low tendency towards agglomeration, controlled crystal size and shape, and good redispersibility.[34,35] According to the authors' best knowledge, there is no data about surfactant-directed microwave processing of ZnO particles. In this study, we employed two types of surfactants, CTAB as the cationic and Pluronic F127 as the non-ionic one. A small amount of surfactants was used, as it has been shown that an excess of surfactants in a solution could led to high viscosities, potentially reducing the mobility of nanoparticles and hindering the self-assembly process.[34,36] We examined in detail the crystal structure, morphological, textural, optical and photo(electro)catalytic properties of microwave (MW) processed ZnO particles. We also discussed the influence of surfactants on the surface-to-bulk defect ratio, and correlated the surface-to-bulk defect ratio with charge separation and radiative recombination of photogenerated electron–hole pairs, as well as their impact on photo(electro)catalytic properties of MW processed ZnO particles.

2. Experimental

2.1. Materials

All chemicals were of analytical grade and used directly as received from the manufacturers without additional purification. Zinc chloride ($ZnCl_2$, purity >99.5, Lach-Ner, Neratovice, Czech Republic) was used as a zinc source, sodium hydroxide (NaOH, purity >98%, Carlo Erba Reagents) as a precipitating agent, cetyltrimethylammonium bromide (CTAB, $C_{19}H_{42}BrN$, Alfa Aesar, Ward Hill, MA, USA) as a cationic surfactant and triblock copolymer Pluronic F127 ($EO_{106}PO_{70}EO_{106}$, Sigma-Aldrich) was employed as a nonionic surfactant. Distilled water was used as the solvent and for powder rinsing, while absolute ethanol (C_2H_5OH, 96%, Zorka Pharma, Serbia) was used for final rinsing.

2.2. Synthesis of catalysts

The powders were prepared by microwave processing of a precipitate. In the first case, 20 mL of 1.75 M NaOH was added dropwise to 100 mL of 0.066 M $ZnCl_2$ solution with continuous stirring for about 20 min. After being stirred at 50 °C for 90 min in total, the as-prepared white precipitate was microwave processed in a domestic oven (2.45 GHz, 130 W) for 5 min. After cooling to room temperature, the suspension was centrifuged at 5000 rpm for 10 min, rinsed at least five times with distilled water and consecutively with absolute ethanol to remove the surface residual of the starting chemical solutions, and air dried in an oven at 60 °C for 24 h.

The same procedure was applied for synthesis of CTAB and Pluronic F127 surface modified ZnO particles except that 0.0472 g of surfactant (CTAB or Pluronic F127) was dissolved in

100 mL of 0.066 M $ZnCl_2$ solution; the surfactant amount was tuned to be 5 wt% with respect to $ZnCl_2$.

Throughout this paper, the powders synthesized without and with the assistance of CTAB and Pluronic F127 surfactants have been designated as ZnO, ZnO/CTAB and ZnO/F127, respectively.

2.3. Characterization

X-ray diffraction (XRD) data were recorded on a Rigaku Ultima IV diffractometer in Bragg–Brentano geometry, with Ni-filtered CuKα radiation (λ = 1.54178 Å). The data were collected over a 2θ range 20–80° with a step of 0.02° and acquisition rate of 2° min^{-1}. The crystal phases were identified by comparing the collected data with those reported in the International Centre for Diffraction Data (ICDD) database. The unit cell parameters were calculated using the least-squares method by the LSUCRI computing program.[37] The crystallite sizes (D) were calculated from XRD line-broadening using the Scherrer equation $D = 0.9\lambda/\beta_m \cos\theta$, where λ is the X-ray wavelength (1.54178 Å); β_m the full width at half maximum (FWHM) for the XRD reflection, and θ the diffraction angle (°).[38,39] Fourier transform infrared (FT-IR) spectra were recorded on a Thermo Scientific™ Nicolet™ iS™10 FT-IR Spectrometer equipped with an attenuated total reflectance (ATR) accessory. ATR/FT-IR measurements were done in the wavenumber region of 400–2000 cm^{-1}, with a resolution of 4 cm^{-1}. Room-temperature μ-Raman spectra were recorded with a DXR Raman microscope (Thermo Scientific, Waltham MA, USA), equipped with an optical microscope and a CCD detector. The spectra were recorded in the frequency interval of 50–3500 cm^{-1} with a resolution of 4 cm^{-1}. The 532 nm line of a diode-pumped solid-state high-brightness laser was used as the excitation source; the laser power was tuned on 10 mW. The morphology of zinc oxide particles was observed by field emission scanning electron microscopy (FE-SEM, Ultra plus, Carl Zeiss, Germany). Samples for FE-SEM analysis were dispersed in water, in an ultrasonic bath, for 5 min; after dispersion a few drops were filtered through a polycarbonate membrane. The membrane was put on carbon tape on an aluminum stub and carbon-coated in order to prevent electron charging. Before analysis, the sample was vacuumed for 15 min. The specific surface area (SSA) and porous properties of photocatalysts were determined based on a N_2 adsorption–desorption isotherm at −195.8 °C using an ASAP 2020 (Micromeritics Instrument Corporation, Norcross, GA, USA). Prior to analysis samples were degassed under reduced pressure at 120 °C for 10 h. The SSA was calculated according to the Brunauer–Emmett–Teller (BET) method from the linear part of the N_2 adsorption isotherm.[40] The total pore volume (V_{total}) was estimated from the adsorbed amount at a relative pressure p/p_0 = 0.998. The volume of mesopores (V_{meso}) and pore size distribution were analysed according to the Barrett–Joyner–Halenda (BJH) method from the desorption branch of the isotherm.[41] The volume of micropores (V_{micro}) was calculated from the alpha-S plot. The particle size distribution in water suspensions was determined by a laser light-scattering particle size analyzer (PSA) (Mastersizer 2000; Malvern Instruments Ltd., Malvern, Worchestershire, U.K.). Prior to measurement, the powders were dispersed in distilled water, using an ultrasonic bath, for 5 min. The measurements were done in a dynamic condition with pump rotation of 1100 rpm. Optical properties were studied by UV-Vis diffuse reflectance (DRS) and photoluminescence (PL) spectroscopy. The UV-Vis DRS were collected using an Agilent Cary 5000 spectrophotometer equipped with a diffuse reflectance accessory. The measurements were performed in the 800–200 nm region, with a 1 nm data interval and 600 nm min^{-1} scan rate, using a commercial PTFE standard for baseline correction. The PL spectra were recorded on a Horiba Jobin Yvon Fluorolog FL3-22 spectrofluorometer using Xe lamp excitation.

2.4. Photo(electro)catalytic tests

The photocatalytic activity of prepared powders was studied by decolorization of methylene blue (MB) dye under direct sunlight illumination. A stock solution with the concentration of 1000 ppm was prepared by dissolving 1.0 g of methylene blue (Methylen blay B extra, E. Merck, Darmstadt, Germany) in 1 L of distilled water. The MB solutions for photocatalytic activity experiments were prepared by diluting the stock solutions to the appropriate concentration. In each experiment, 0.1 g of the prepared powder was mixed with 100 mL of the MB aqueous solution with a concentration of 10 ppm in a beaker. To distinguish the efficiency of degradation from adsorption, prior to illumination the suspension was magnetically stirred for 1 h in dark to establish the adsorption–desorption equilibrium. After equilibrium was established, the concentration of MB was measured and taken as the initial concentration C_o. During illumination stirring was maintained to keep the mixture in suspension. At specific time intervals, 3 mL aliquots were withdrawn and centrifuged (7000 rpm, 5 min) to remove particles from the solution before absorbance measurements. Solution concentrations were monitored by a GBC Cintra UV-Vis spectrophotometer in the wavelength range of 450–750 nm; the concentration of MB was calculated according to the absorbance value at 665 nm. The experiments were done under direct sunlight illumination between 12 a.m. and 15 p.m. during the month of May 2018 and at ambient temperature (25 to 28 °C). The intensity of light was measured by a PeakTech 5165 Digital-Lux-Meter and it varied between 900 and 1100 lux.

Photoelectrocatalytic (PEC) efficiency was investigated using linear sweep voltammetry (LSV), chronoamperometric (CA) and electrochemical impedance spectroscopy (EIS) measurements. The PEC measurements were performed on a Gamry PCI4/750 using a three-electrode quartz cell consisting of a working electrode, platinum foil as the counter electrode and a saturated calomel electrode (SCE) as the reference electrode. The working electrode paste was prepared by mixing 90 wt% of zinc oxide powder as an active material with 10 wt% polyvinylidene fluoride (PVDF) binder in *N*-methyl-2-pyrrolidone (NMP) solvent. This slurry was homogenized for 1 h in an ultrasonic bath, and subsequently coated on FTO glass (Sigma-Aldrich 20 Ω cm^{-2}) as a thin film. To evaporate the solvent, the electrode was dried under vacuum at 170 °C for 4 h. The surface area of the working electrode was 3 cm^2. In all electrochemical measurements, an

aqueous solution of 0.1 M Na_2SO_4 was used as the electrolyte. Dark conditions during measurements were provided by protecting the cell from light. An Osram Ultra-Vitalux 300 W lamp was used as the light source. The distance between the light source and the cell was adjusted to 20 cm, yielding about 90 mW cm^{-2} illumination intensity. LSV was measured with a scan rate of 20 mV s^{-1} in the voltage range between 0.2 V and 1.5 V *vs.* SCE. The impedance diagrams of ZnO samples were measured in the frequency interval from 10^5 to 0.01 Hz, using an AC voltage amplitude of 5 mV at a fixed potential of 1.5 V *vs.* SCE. The impedance data were fitted to the electrical analogue under study using *Z*-View2 (version 3.5) software. The chronoamperometric study was performed under chopped light illumination in a constant time interval of 60 s at 1.5 V *vs.* SCE.

3. Results and discussion

3.1. The influence of CTAB and F127 on the crystal structure, morphology and textural properties of ZnO particles

It has been demonstrated that the photocatalytic activity of metal-oxide photocatalysts for both water purification and overall water splitting, comprehensively depends on the crystallinity, crystallite size and polarity, as well as the particle size and textural properties.[13,34,42,43] In particular, for ZnO-based photocatalytic particles, it has been established that hexagonal platelike crystals exhibit 5-fold better photocatalytic activity than rodlike ones.[34,42,43] An improved activity of platelike crystals can be explained by ZnO crystalline structure. ZnO has a wurtzite crystalline structure with layer contains all positive Zn^{2+} ions or all negative O^{2-} ions stack alternatively along the [0001] direction, resulting in the Zn-terminated (0001) and O-terminated $(000\bar{1})$ polar planes;[43] an illustrative stacking model of ZnO with a wurtzite crystalline structure is presented in Fig. 1(a). The terminal polar planes (0001) and $(000\bar{1})$ were reported to be much more active in photocatalysis as compared to the nonpolar facets perpendicular to them (for example $1\bar{1}00$, or $01\bar{1}0$), mainly due to a higher density of defects such as oxygen vacancies.[34] Surfactants can significantly affect crystallite polarity, morphology and specific surface area of ZnO particles prepared by the hydrothermal method.[34] Up to now, there has been no data about the influence of surfactants on the crystal structure, morphology and textural properties of ZnO particles synthesized by fast, energy-effective microwave processing. The XRD patterns of microwave processed ZnO, ZnO/CTAB and ZnO/F127 particles are shown in Fig. 1(b). The patterns indicate highly crystalline particles with a wurtzite-type hexagonal symmetry, without other crystal phases or impurities (ICDD no. 89-0510) (the existence of solely Zn and O atoms in the ZnO samples is confirmed by EDX analysis). The unit cell parameters calculated for ZnO particles, synthesized without the aid of surfactants, were found to be $a = b = 3.2509(6)$ Å, $c = 5.2103(2)$ Å, $V = 47.69(2)$ Å^3 which is in good agreement with the parameters for ZnO crystals with a wurtzite-type hexagonal structure (ICDD no. 89-0510). To determine the orientation of crystal growth, crystallite size was calculated for three specific crystallographic directions [100], [002] and [101] and was found to be 19.9, 18.1 and 18.0 nm, respectively, indicating an almost isotropic nano-crystallites growth. The calculated polarity value, $I_{(002)}/I_{(100)}$, was 1.27. The unit cell parameters, crystallite sizes and polarity were also calculated for ZnO/CTAB and ZnO/F127; the calculated values are listed in Table 1. As can be noticed, neither the presence of surfactants nor their type, cationic or non-ionic, influenced the lattice parameters. However, the crystallite size and isotropy were affected by the presence of surfactants. A more profound effect on crystallite growth and polarity was observed when CTAB was used; $I_{(002)}/I_{(100)} = 1.11$ indicating a well-developed polar (0001) plane (the plane normal to the [0001]-axis, Fig. 1(c)) with a hexagonal platelike morphology, implicating that ZnO/CTAB could be very effective towards the decolorization of methylene blue.[34] We demonstrated that a relatively small amount of surfactants influenced the crystallite size and polarity despite the short time period (5 min) of microwave irradiation, leading to a fast crystallization of the $Zn(OH)_2$ precursor into the ZnO phase.[30]

The representative FE-SEM micrographs of MW processed zinc oxide particles are shown in Fig. 2. As can be seen, in the ZnO powder processed without surfactants nanocrystallites are organized in cone-shaped particles with a uniform size and morphology. The average length of particles, deduced from the image by measuring more than 250 particles employing the SemAfore digital slow scan image recording system, is 93 nm. The uniformity of zinc oxide particles deteriorated when CTAB was used. The ZnO/CTAB powder consisted of spheroidal particles with an estimated average diameter of 58 nm; the particles were scatteredly organized in thin platelike aggregates with lengths between 220 and 670 nm and an average thickness of *cc*. 30 nm. The ZnO/F127 powder consisted of cone-shaped particles, similar to those in ZnO but with a reduced average length, estimated to about 80 nm. The particle size distributions determined from the micrographs using the computing program are included in Fig. 2 as insets. The particle size distributions with characteristic parameters ($d(0.1)$, $d(0.5)$, $d(0.9)$ and *span*) determined by laser diffraction scattering are presented in the bottom part of Fig. 2. The particles size distributions are presented over a number since it gives insight into the statistically predominant particles. The characteristic parameters measured for ZnO, ZnO/CTAB and ZnO/F127

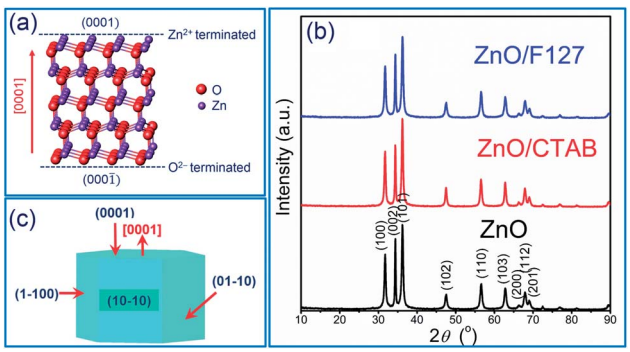

Fig. 1 (a) Illustration of ZnO wurtzite crystalline structure, (b) XRD patterns of microwave processed ZnO particles, and (c) scheme of ZnO crystallite.

Table 1 Unit cell parameters with standard deviations, crystallite sizes in specific crystallographic directions, polarity values and Raman intensity ratio with specific band position

	Unit cell parameters			Crystallites size, D (nm)				Raman	
Sample	$a = b$ (Å)	c (Å)	V (Å^3)	D_{100}	D_{002}	D_{101}	$I_{(002)}/I_{(100)}$	I_{440}/I_{570}	E_{2H} (cm^{-1})
ZnO	3.2509(6)	5.2103(2)	47.69(2)	19.9	18.1	18.0	1.27	1.165	434.6
ZnO/CTAB	3.2519(7)	5.2093(2)	47.71(2)	21.0	19.8	18.6	1.11	1.295	436.5
ZnO/F127	3.2513(7)	5.2114(3)	47.71(2)	19.6	18.0	17.1	1.22	1.195	436.5

implicate that surfactants slightly influenced the particle size distributions; for example, $d(0.5)$ varied from 285 nm for ZnO, to 336 nm for ZnO/CTAB and 270 nm for ZnO/F127, revealing the same trend as the values for the average crystallite size and the particle size distributions determined from the micrographs, ZnO/F127 < ZnO < ZnO/CTAB. As expected, the average particle sizes measured in water suspensions were about threefold larger than those deduced from FE-SEM images, which is due to both the hydrodynamic diameter and particle sticking in dynamic fluid conditions.[9]

It is known that the presence of CTAB in different concentrations (from 0.1 to 0.8 M) can greatly change the shape of ZnO crystals obtained by hydrothermal or solvothermal synthesis.[44] In this study we established that even small amounts of surfactant, 0.0013 mol L^{-1} CTAB or 0.0029 mol L^{-1} Pluronic F127, affected the shape and size of microwave processed zinc oxide particles. We also showed that platelike sub-micrometer sized agglomerates could be prepared even with energy-efficient MW processing.

The textural properties of metal-oxide particles influence their catalytic properties; more accurately, a larger surface area and a larger pore volume of the samples provided a larger number of active sites for photocatalytic reactions.[45] Different surfactants are often used to control the morphology and texture of hydrothermally processed ZnO particles.[46–49] The influence of surfactants on the textural properties of microwave processed zinc oxide particles are listed in Table 2. The specific surface area of ZnO particles processed without the aid of surfactants was 19.1 m^2 g^{-1}, the total pore volume was found to be 0.0710 cm^3 g^{-1} with about 97% of mesopores and average pore diameter 14.2 nm. The BET results show that even a small amount of CTAB as a surfactant enlarged SSA for more than 60%, *i.e.* to 24.8 m^2 g^{-1}; the total pore volume was 0.1147 cm^3 g^{-1}, mesopores were also predominant while the average pore diameter was increased to 20.5 nm. The BET surface area of ZnO/F127 was 15.5 m^2 g^{-1}, the total pore volume was 0.0723 cm^3 g^{-1} with more than 95% of mesopores and an average pore diameter of 25.5 nm. These values indicate profound effects of CTAB on all textural properties: SSA, the total pore volume, and the average pore diameter, while the same amount of Pluronic F127 slightly decreased SSA, had no influence on the total pore volume, but played an important role in the development of larger mesopores. Accordingly, both samples synthesized with the aid of surfactants had good catalytic potential.

ATR/FT-IR spectra were employed to inspect functional groups in ZnO particles and identify possible residues of the reagents used for MW processing. As can be seen from Fig. 3, all the spectra are practically identical. The most prominent band

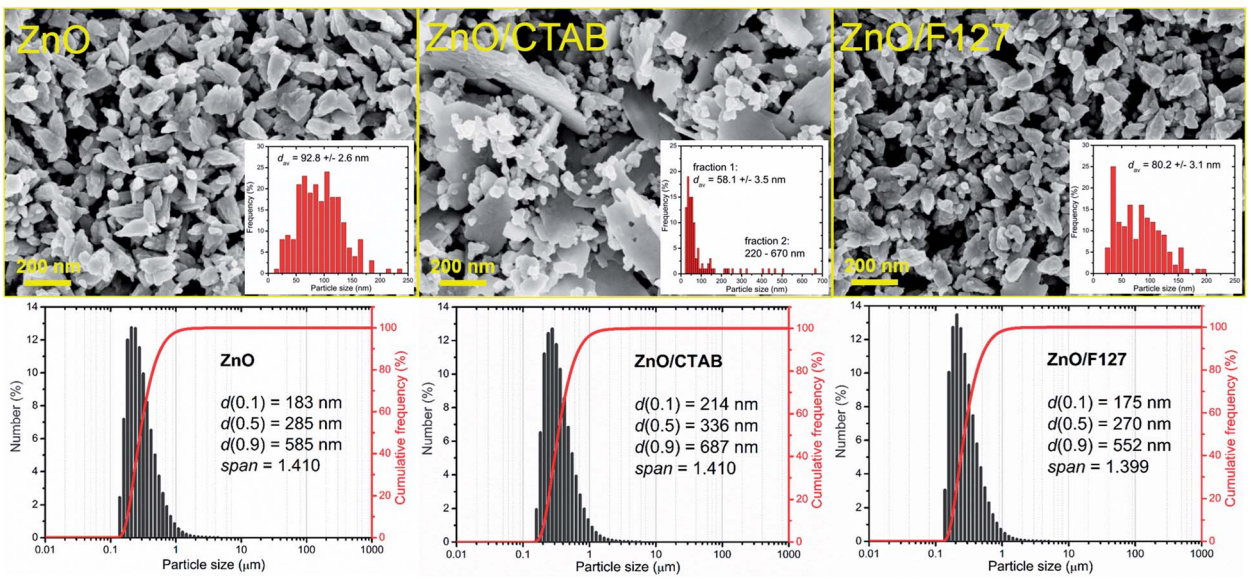

Fig. 2 FE-SEM images of microwave processed ZnO particles, with particles size distribution deduced from the images as insets, and particle size distribution determined by laser diffraction from water suspensions (bottom).

Table 2 Textural (SSA, volume and size of pores), and morphological properties of ZnO particles

Sample	S_{BET}[a] ($m^2\ g^{-1}$)	V_{total}[b] ($cm^3\ g^{-1}$)	V_{meso}[c] ($cm^3\ g^{-1}$)	V_{micro}[d] ($cm^3\ g^{-1}$)	r_{av}[e] (nm)	$d_{av,FE\text{-}SEM}$[f] (nm)	$d_N(0.5)_{PSA}$[g] (nm)	Particles shape
ZnO	19.1	0.0710	0.0687	0.0054	14.2	92.7	285	Conelike
ZnO/CTAB	24.8	0.1147	0.1121	0.0088	20.5	355.0	336	Platelike
ZnO/F127	15.5	0.0732	0.0698	0.0062	25.7	80.2	270	Conelike

[a] S_{BET} – BET specific surface area. [b] V_{total} – total pore volume. [c] V_{meso} – volume of mesopores (2–50 nm). [d] V_{micro} – volume of micropores (<2 nm). [e] r_{av} – BJH adsorption average pore diameter. [f] d_{av} – average particle size determined from FE-SEM images. [g] $d_N(0.5)_{PSA}$ – average particle size (based on number) determined by PSA.

is in the 400–600 cm^{-1} region and it is attributed to Zn–O vibrations in the ZnO lattice.[50] The weak peak centered at 890 cm^{-1} can be assigned to –C–H bending vibrations; it is most probably due to the residue of ethanol used to rinse the sample after microwave processing. The broad bands in the regions 1320–1575 and 3200–3550 cm^{-1} are attributed to bending and stretching vibrations, respectively, of O–H groups from the adsorbed water molecules hydrogen bonded to the surface of zinc oxide particles.[51,52] Very weak intensities and relatively small peak areas indicate that a negligible amount of hydroxyl groups is adsorbed on the surface of ZnO particles and that we are dealing with ZnO rather than $Zn(OH)_2$.[51] No residues of either the processing reagents or surfactants can be observed.

The room-temperature μ-Raman spectra, used to study the influence of surfactants on lattice defects in microwave processed ZnO particles, are shown in Fig. 4(a). The most intensive band at 98 cm^{-1}, assigned as E_{2L}, is characteristic of the wurtzite crystal structure and can be attributed to vibrations of the zinc sublattice in ZnO.[30,53,54] The low intensity peak centered near 200 cm^{-1} and a sharp peak at 327 cm^{-1} are attributed to the second-order phonon mode $2E_{2L}$ and the multi phonon mode E_{2H}–E_{2L}, respectively.[55] The weak shoulder near 380 cm^{-1} (marked with a dark cyan triangle in Fig. 4(a)) is attributed to A_1 (TO). The second weak shoulder at 410 cm^{-1} (marked with a pink asterisk in Fig. 4(a)) corresponds to the E_1 (TO) mode; it indicates that ZnO crystallites have propagation in a direction other than the *c*-axis typical of ZnO particles.[56] This is in accordance with the (almost) isotropic crystallite geometry calculated from the XRD data for the most characteristic crystallographic directions (Table 1). The peak centered at 435 cm^{-1} is due to the E_{2H} mode and it is assigned to oxygen vibrations.[55] According to literature data, the asymmetry of the E_{2H} peak points to lattice disorder while its intensity indicates crystallinity.[57,58] In the Raman spectrum of MW processed ZnO nanocrystals, a relatively high intensity of the E_{2H} peak indicates a good crystallinity which is in accordance with the crystallinity of about 80% calculated from the XRD data. A wide optical phonon band in the 510–740 cm^{-1} interval holds two peaks; the one centered near 570 cm^{-1} represents A_1 (LO) and E_1 (LO) modes, whereas the other, at 635 cm^{-1} represents a combination of acoustic and optical modes (TA + LO). The A_1 (LO) mode is associated with the bulk defects: oxygen vacancies, zinc interstitials or defect complexes containing both.[55] It has been shown that the presence of impurities and/or defects strongly influences these modes, especially E_1 (LO).[58,59] The relatively high-intensity of the A_1 (LO) + E_1 (LO) modes in the Raman spectrum of the ZnO sample (Fig. 4(a)) points to a relatively large density of intrinsic bulk defects (oxygen vacancies and zinc interstities); these bulk defects were incited by rapid crystallization driven by microwave irradiation.[30] The A_1 (LO) mode is accompanied with a weak band at 483 cm^{-1} (marked with an orange circle), which is assigned as the interfacial surface phonon mode 2LA.[55] The wide band in the wavenumber region 1090−1150 cm^{-1} is attributed to the optical overtone 2LO, namely to $2A_1$ (LO) and $2E_1$ (LO).

As Fig. 4(a) shows, all vibrational modes appearing in the Raman spectra of ZnO particles processed with the aid of surfactants correspond well to those for the bare one. However, we found that surfactants caused a red shift of the E_{2H} mode (Fig. 4(b) & Table 1). Since the E_{2H} mode is mainly due to the motion of oxygen atoms perpendicular to the *c*-axis of ZnO crystals, any change on the bond bending caused by the tensile

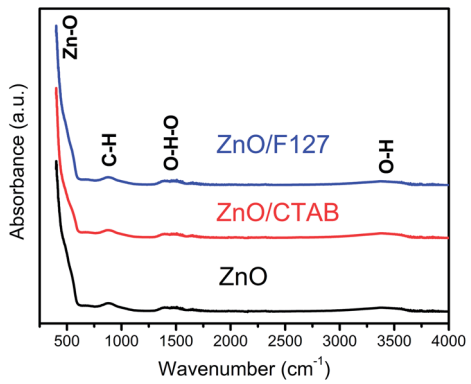

Fig. 3 FTIR spectra of microwave processed ZnO particles.

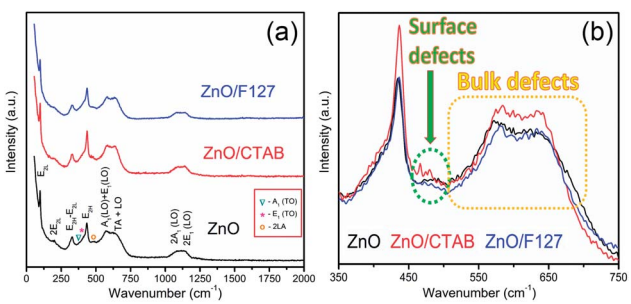

Fig. 4 (a) Raman spectra of microwave processed ZnO particles, and (b) expanded 350–750 cm^{-1} region of E_{2H} and A_1 (LO) + E_1 (LO) mode.

strain along the *c*-axis results in a red shift of the E_{2H} mode.[60] The slight red shift of the E_{2H} mode, from 434.6 to 436.5 cm^{-1}, indicates an increase of the tensile strain caused by a decrease of oxygen vacancies compared to bare ZnO. As expected, since oxygen atoms are less massive than zinc atoms, redistribution of electron density due to defects has a stronger influence on the oxygen sublattice, represented by the E_{2H} mode, than on the vibrations of the zinc sublattice assigned as E_{2L}. Another impact of the surfactants on the Raman spectra of MW processed ZnO particles is proved by the relationship between intensities of the E_{2H} mode to the A_1 (LO) + E_1 (LO) mode, Fig. 4(b) and Table 1. An increase of the I_{440}/I_{570} intensity ratio confirms the decrease of the concentration of intrinsic lattice defects. The decreased amount of oxygen vacancies in the crystal lattices of ZnO/CTAB and ZnO/F127, compared to bare ZnO, can be attributed to the *in situ* action of polymers as passivating agents.[61] The bromide anions of CTAB or oxygen ions of Pluronic can fill up the singly (V_O^+) or doubly (V_O^{++}) charged states of oxygen vacancies in the ZnO lattice.[62]

3.2. The influence of CTAB and F127 on the optical properties of ZnO particles

To investigate the effect of the cationic and non-ionic surfactants on the optical properties of ZnO particles synthesized by MW processing, UV-Vis DR and PL spectra were recorded. UV-Vis DRS plots show characteristic reflectance curves with the adsorption edge near 370 nm, Fig. 5(a). While all samples absorbed more than 95% of UV light, they showed a slightly different absorption capacity of visible light. Actually, the ZnO sample revealed the highest reflectance; compared to ZnO/CTAB and ZnO/F127, ΔR increased from 5 to 10% in the 400–800 nm spectral region. The absorption capacity varied in the following manner: ZnO < ZnO/F127 < ZnO/CTAB. The different absorption capacity in the visible spectral region could be attributed to both different morphologies of ZnO particles and the density of surface defects. As previously shown, particles with a larger diameter or thickness have a longer optical path for light transport, resulting in a greater absorption capacity; particle size can influenced the capacity of visible-light absorption even without affecting the band gap energy.[48,63] Surface defects can additionally enhance visible light absorption.[30] To determine both, direct and indirect band gap energies (E_{bg}) of ZnO particles the Kubelka–Munk method was employed.[30] The diffuse reflectance R is related to the Kubelka–Munk function $F(R)$ by eqn (1):

$$F(R) = \frac{(1-R)^2}{2R} \quad (1)$$

where R is the percentage reflectance. After finding the $F(R)$ value from eqn (1) graphs of $[F(R) \times E]^2$ and $[F(R) \times E]^{1/2}$ *vs.* energy E (eV) were plotted. The band gap energies were estimated by extrapolation of the linear part of the curves to $[F(R) \times E]^2$ *i.e.* $[F(R) \times E]^{1/2}$ to 0, Fig. 5(b) and (c). The estimated values for the direct band gaps were 3.36 eV for ZnO and ZnO/F127, and 3.34 eV for ZnO/CTAB, which is in accordance with the one for bulk ZnO (3.37 eV).[64] The estimated values for the indirect bandgaps were 3.23, 3.22 and 3.24 eV for ZnO, ZnO/CTAB and ZnO/F127, respectively. Thus, CTAB caused a slight shift of the band gap energy toward the visible light region while the same weight amount of Pluronic had no influence on the band gap of zinc oxide particles.

The photoluminescence spectra of ZnO-based materials commonly exhibit UV emission due to exciton recombination which is accompanied with defect related visible emission.[65] Among a variety of point defects, the main types in ZnO are zinc interstitials (Zn_i) and oxygen vacancies (V_O); the former are surface defects, also known as shallow donors, while the latter make deep-level *i.e.* bulk defects.[66] To ascertain the influence of surfactants used in microwave processing on the surface-to-bulk defect ratio in the synthesized ZnO particles, room temperature PL spectra were recorded with the excitation wavelength of 290 nm, Fig. 6(a). The most peculiar observation in the PL spectra is the absence of the near band edge (NBE) emission of ZnO, which is usually a sharp band near 380 nm, originating from the recombination of photo-induced charge carriers through an exciton–exciton collision process.[67] The absence of the NBE emission in PL spectra indicates that recombination of photo-induced electrons and holes in the ZnO particles can be efficiently inhibited by microwave processing.[30] All PL spectra show a similar pattern; two emission bands appear: one in the 370–470 nm region and the other in the wide spectral region, from 470 to 700 nm, and they are attributed to surface and deep-level defects, respectively. As can be seen from Fig. 6(a), the type of surfactant used in MW processing affected

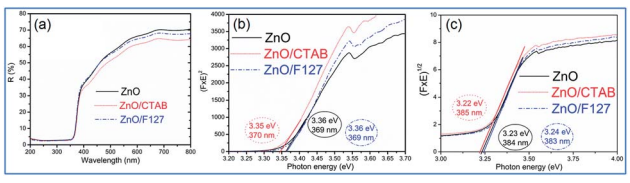

Fig. 5 (a) UV-Vis DR spectra of microwave processed ZnO particles, (b) Kubelka–Munk plots for direct, and (c) indirect bandgap semiconductors.

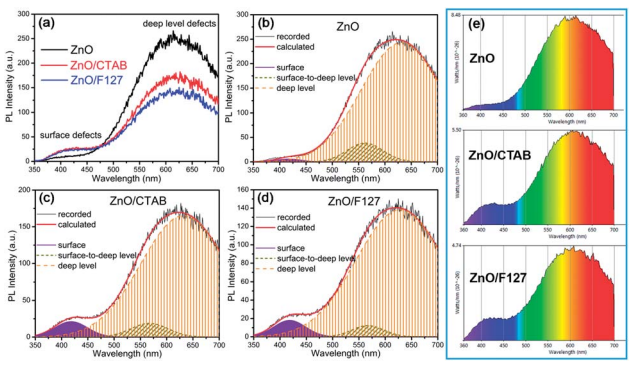

Fig. 6 (a) Photoluminescence spectra of microwave processed ZnO particles under excitation at 290 nm, (b–d) PL spectra deconvoluted with a Gaussian function, (e) PL emission spectra in the visible spectral range which is distinguished by a deconvolution.

the PL intensity, as well as the intensity of the surface-to-bulk defect ratio, attributed to the I_{620}/I_{410} ratio. To reveal the precise position, intensity and area (%) of the emission bands, the PL spectra were mathematically deconvoluted. Before fitting, for the sake of comparison, the areas of the PL spectra were normalized to 1. Deconvolution of the PL spectra was successfully done by three Gaussian components centered near 420, 570, and 630 nm, and attributed to the violet-blue, green-yellow and orange-red emissions, respectively, Fig. 6(b)–(d). Fig. 6(e) is an illustrative representation of the PL emission spectra in the visible spectral range which is distinguished by deconvolution. The data obtained by deconvolution are listed in Table 3. There is still controversy about the origin of the violet(-blue) emission, as it has been reported to originate from Zn_i but also from V_{Zn}.[68] The main assumption is that the probability of forming V_{Zn} is slight since the enthalpy of V_{Zn} defects is higher than the enthalpy of Zn_i defects. In this paper, the violet-blue emission band centered near 420 nm is attributed to the existence of interstitial zinc; it is caused by the electron transition from the interstitial and extended interstitial levels of zinc to the valence band.[66–68] To be more precise, transition from the interstitial to the valence band is typical of violet emission, while transition from the extended Zn_i states, which are slightly below the simple Zn_i state, to the valence band is typical of blue emission. The band centered at 560 nm corresponds to the green-yellow emission correlated to the existence of both surface and deep-level defects. Actually, the green emission is due to the transition from the conduction band to the deep levels of the doubly charged oxygen vacancy states (V_O^{++}), while the yellow emission is induced by the transition from the Zn_i energy level to the deep-levels of V_O^{++}.[66] The most intensive and the broadest band in the orange-red spectral region centered near 630 nm is correlated to the existence of zinc interstitials and oxygen interstitials; it is probably due to the transition from the Zn_i level to the O_i level in ZnO.[69,70] The energy levels of intrinsic defects in ZnO have been calculated using the full-potential linear muffin-tin orbital method;[71,72] the position of the Zn_i level is theoretically located at 0.22 eV below the conduction band while the position of the O_i level is located approximately at 2.28 eV below the conduction band. It is expected that the transition from the Zn_i energy level to the O_i energy level is approximately 2.06 eV, which is in good agreement with the orange-red peaks centered approximately at 1.97 eV. The energy band diagram (Fig. 7), based on the theoretically calculated energy values for different point defects and emission energies deduced after deconvolution of the PL spectra, indicates the most probable defects in the structure of microwave processed zinc oxide particles.

The low-intensity violet-blue emission and the strong orange-red emission, including the green-yellow emission, in the PL spectrum of ZnO indicate a negligible concentration of Zn interstitial defects and a high concentration of both oxygen vacancies and oxygen interstitials. As explained in our previous paper, a large amount of intrinsic bulk defects is due to rapid crystallization caused by the high energy provided to the precipitated precursor *via* microwave irradiation.[30] The intensity and the surface area of the emission bands in the PL spectrum of ZnO/CTAB are somewhat different from those in the PL spectrum of ZnO. The violet-blue emission indicates a larger concentration of surface defects while the sum of green-yellow and orange-red emissions indicates a reduced concentration of oxygen vacancies and interstitials. These results are in agreement with the Raman spectroscopy data (Fig. 4, Table 1), which reveal an increase in crystallinity simultaneously with a reduced concentration of oxygen vacancies as a result of bonding between bromide anions in CTAB with V_O^+ or V_O^{++} in the ZnO lattice. The PL spectrum of ZnO/F127 is almost the same as the corresponding spectrum of ZnO/CTAB, though the surface-to-bulk area ratio is somewhat different. In this case, oxygen ions of Pluronic F127 were involved in the neutralization of V_O^+ or V_O^{++} in the ZnO lattice. The recorded PL spectra with additional deconvolution confirm the profound effects of surfactants (used in MW processing) on the relative surface-to-bulk defect ratio. An illustrative representation of the impact of surfactants on the defect chemistry and radiative recombination in the microwave processed zinc oxide particles is given by the chromaticity (CIE 1931) plot in the (x, y) coordinate system, Fig. 8. The chromaticity coordinates are (0.4724, 0.4559), (0.4474, 0.4213), and (0.4393, 0.4202) with correlated color temperatures 2860, 2967, and 3088 K for ZnO, ZnO/CTAB, and ZnO/F127, respectively. This CIE plot displaying ZnO particles with color tunability, indicates great possibilities of the

Table 3 Position, intensity and area of emission bands in PL spectra obtained after deconvolution by a Gaussian function

		Emission		
Sample	Peak	Violet-blue	Green-yellow	Orange-red
ZnO	Position (nm)	417	562	632
	Intensity	5.72	38.4	243.0
	Area (%)	0.81	7.88	91.31
ZnO/CTAB	Position (nm)	418	567	633
	Intensity	21.1	18.7	165.3
	Area (%)	5.36	5.33	89.10
ZnO/F127	Position (nm)	418	567	628
	Intensity	17.9	12.2	138.5
	Area (%)	5.22	3.63	91.14

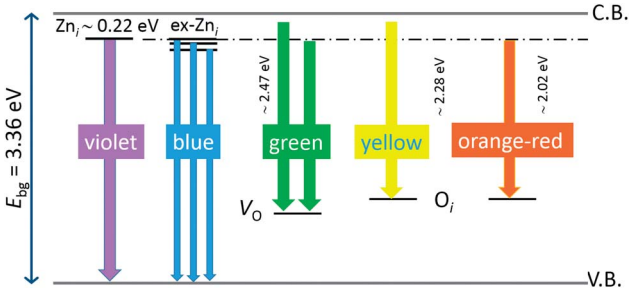

Fig. 7 Schematic band energy diagram based on the full potential linear muffin-tin orbital method,[71,72] and the recorded data with denoted possible point defects in the microwave processed ZnO particles.

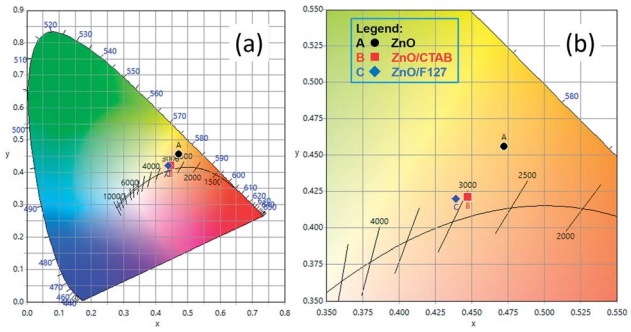

Fig. 8 (a) The CIE 1931 *x*, *y* chromaticity space of microwave processed ZnO particles and (b) magnified image with CRI values.

microwave processing of ZnO by merely varying surfactants or polymers. ZnO particles synthesized in this way may be applied as white light emitting devices (WLEDs).[73]

It is noteworthy that apart from the nature of point defects, PL also reflects band structures: in direct bandgap materials, the PL spectrum is narrow with a high intensity, while in indirect bandgap materials the PL spectrum can be broad with small intensity peaks. Therefore, the PL spectra imply that microwave processed ZnO materials have an indirect bandgap, which is more probably due to a large amount of point defects.

3.3. The influence of CTAB and F127 on the photocatalytic properties of ZnO particles

As we deduced from the PL spectra, a high efficiency of charge separation is achieved in the microwave processed ZnO particles, resulting in a great potential for photocatalytic activity. As a simple check of photocatalytic activity, MW processed ZnO powders were tested for decolorization of methylene blue (as a model system) under direct sunlight illumination. Fig. 9(a) reveals the efficiency of the photocatalytic degradation of MB dye in the presence of the microwave processed ZnO powders. ZnO/CTAB and ZnO/F127 showed a 100% efficiency after 2 h of direct sunlight illumination, while the efficiency of ZnO was just 67% after 5 hours of illumination. The time necessary to decolorize 50% of the dye ($t_{1/2}$) was calculated from the kinetic plots, Fig. 9(b); the calculated $t_{1/2}$ values for ZnO, ZnO/CTAB and ZnO/F127 are equal to 135, 26.42 and 32.92 min, respectively. The photocatalytic activities of different ZnO-based materials were compared in terms of the rate constant of degradation of some typical dyes, and are listed in Table 4.

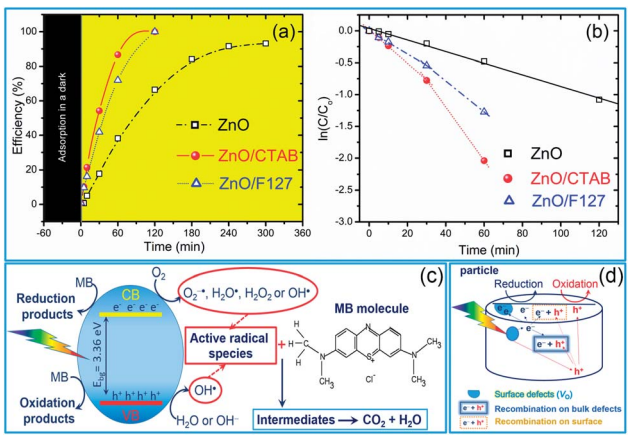

Fig. 9 (a) Photocatalytic efficiency, (b) appropriate first-order reaction kinetic plots for de-colorization of $[MB]_i = 10$ ppm in the presence of microwave processed ZnO particles under natural sunlight illumination, (c) illustration of the reaction scheme for MB photodegradation on ideal ZnO crystal, and (d) illustration of exciton recombination pathways on ZnO with surface and bulk defects.

Generally, photocatalytic activity is driven by crystallinity, optical properties, specific surface area, particle size and morphology. In particular a higher surface-to-bulk defect ratio and larger particle sizes are expected to increase the photocatalytic activity of ZnO materials. A higher surface-to-bulk defect ratio diminishes the probability of recombination of photoexcited electrons and holes, simultaneously enhancing photocatalytic activity; while larger particles have a better absorption capacity. In the case of microwave processed ZnO particles, an excellent photocatalytic activity of ZnO/CTAB can be attributed to: (a) the larger surface area and larger pore volume (Table 2), providing a larger number of active sites for photocatalytic reactions,[45] (b) a specific platelike particle morphology with an average size of about 550 nm enhanced the absorption capacity of visible light, ZnO/CTAB particles exhibited ~5% higher absorbance capacity than ZnO particles (Fig. 5), (c) the increased surface-to-bulk defect ratio (Fig. 4, Table 2) hindered recombination of photogenerated electrons and holes. Both surfactants decreased the concentration of bulk oxygen vacancies, while sensitizing the surfaces.

It has been shown that mechanism of MB photodegradation depends on point defects in photocatalysts.[81,82] Generally, a reaction pathway for MB degradation on a photocatalyst is very complex, it assume series of reactions starting with photoexcitation eqn (2). Actually, when ZnO absorb light with energy equal or greater than the band gap of the semiconductor, electrons are excited from the valence band to the conduction band. In following, the photogenerated holes (h^+) and electrons (e^-) migrate from bulk to surface. The photogenerated holes at the VB react with water molecules adsorbed at the particle surface to produce hydroxyl radical $OH^\bullet$ eqn (3), while electrons in CB react with oxygen molecules generating anionic superoxide radical $O_2^{-\bullet}$ eqn (4). In further steps radicals can be transformed in highly reactive $OH^\bullet$ eqn (5)–(8).[81,82]

$$ZnO + h\nu \rightarrow ZnO\ (e^-\ (CB) + h^+\ (VB)) \quad (2)$$

$$h^+\ (VB) + H_2O \text{ or } OH^- \rightarrow OH^\bullet + H^+ \quad (3)$$

$$e^-\ (CB) + O_2 \rightarrow O_2^{-\bullet} \quad (4)$$

$$O_2^{-\bullet} + H^+ \rightleftarrows HO_2^\bullet \quad (5)$$

$$2HO_2^\bullet \rightarrow H_2O_2 + O_2 \quad (6)$$

$$2HO_2^\bullet + 2H^+ \rightarrow H_2O_2 + 2OH^\bullet \quad (7)$$

$$H_2O_2 \rightarrow 2OH^\bullet \quad (8)$$

Table 4 Reaction rate constants for different ZnO-based photocatalysts

Sample	Rate constant (min^{-1})	Degradation parameters	Ref.
ZnO-600	0.0203	MO under UV light	74
Ag-ZnO-600	0.06838	MO under UV light	74
Ce-ZnO/CNT	0.00579	MB under UV light	75
Ce-ZnO	0.00211	MB under UV light	75
ZnO	0.00072	MB under UV light	75
ZnO	0.027	MB under UV light	76
ZnO rodlike particles	0.06329	RhB under UV light	77
ZnO ricelike particles	0.0431	RhB under UV light	77
ZnO disclike particles	0.02448	RhB under UV light	77
ZnO	0.22	MB under UV light	78
ZnO, 180 min milled	0.0097	MB under UV light	78
ZnO nanospheres	0.017	MO under Vis light	79
ZnO hollow nanospheres	0.0288	MO under Vis light	79
ZnO yolk–shell nanospheres	0.0321	MO under Vis light	79
ZnO	0.0023	MB under UV light	80
ZnO/PEO-2	0.0042	MB under sunlight	30
ZnO/PEO-6	0.0100	MB under sunlight	30
ZnO/PEO-9	0.0057	MB under sunlight	30
ZnO	0.0356	MB under UV light	9
ma-ZnO/SnO_2	0.0736	MB under UV light	9
ZnO/SnO_2-400	0.0638	MB under UV light	9
ZnO/SnO_2-700	0.00342	MB under UV light	9
ZnO	0.136	MB under sunlight	9
ma-ZnO/SnO_2	0.180	MB under sunlight	9
ZnO/SnO_2-400	0.0440	MB under sunlight	9
ZnO/SnO_2-700	0.0120	MB under sunlight	9
ZnO	0.0051	MB under sunlight	This work
ZnO/CTAB	0.0262	MB under sunlight	This work
ZnO/F127	0.0210	MB under sunlight	This work

Degradation of MB molecule obey *via* reaction with radicals (9), especially with $O_2^{-\bullet}$, $HO_2^{\bullet}$, and $OH^{\bullet}$ as highly reactive ones, and may be accompanied with oxidation (10) and reduction (11) processes on the surface of the photoexcited catalysts.[81] After several steps and intermediates, the final products of MB photodegradation are CO_2, H_2O and inorganic molecules (9).[82]

$$\text{MB dye} + \text{reactive radicals} \rightarrow \text{MB dye intermediates} + \text{reactive radicals} \rightarrow \ldots \rightarrow CO_2 + H_2O + \text{inorganic molecules} \quad (9)$$

$$\text{MB dye} + h^+ (\text{VB}) \rightarrow \text{oxidation products} \quad (10)$$

$$\text{MB dye} + e^- (\text{CB}) \rightarrow \text{reduction products} \quad (11)$$

The proposed photodegradation mechanism of MB dye on ZnO catalysts under direct sunlight irradiation is illustratively represented in Fig. 9(c). Mechanism of radical formation and further dye degradation depends on the surface-to-bulk defect ratio. In the case of a ZnO crystal free of any defects electron–hole recombination is in competition with charge transfer to adsorbed species. Mechanistic studies demonstrate that the majority of photogenerated electrons and holes recombine, resulting in a moderate photoactivation efficiency. The recombination can occurs in both the bulk and the surface.[83] Theoretical calculations and experimental studies have shown that the surface defects can trap the photogenerated holes, helping the separation of photogenerated electron–hole pairs and hindering the recombination. What's more, the photogenerated holes trapped by surface defects are ready to react with electron donors (*e.g.* OH^-) and the photocatalytic reaction can be greatly promoted.[83] Although, the defects in the bulk can act as the recombination centers leading to the deterioration of photocatalytic efficiency.[84–86] With all the other influencing factors, surface defects play a significant role in the photodegradation mechanism. Fig. 9(d) illustrate an general exciton recombination pathways on ZnO crystal with surface and bulk defects. Fig. 10 illustrate crystal structures of the ZnO, ZnO/CTAB, and ZnO/F127, pointing to different surface-to-bulk defect ratio.

An electrochemical impedance spectroscopy analysis was carried out to investigate the charge transfer and charge recombination processes when microwave processed ZnO were

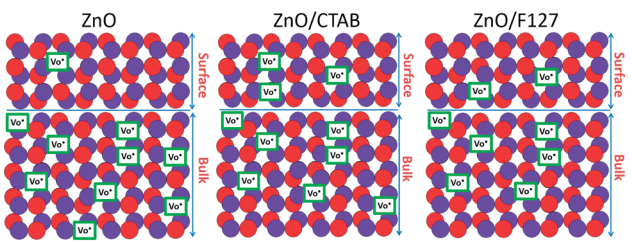

Fig. 10 Illustration of ZnO, ZnO/CTAB and ZnO/F127 crystal structures.

used as photoanodes. The LSV of ZnO photoanodes, recorded in dark conditions and under illumination, are shown in Fig. 11(a). The current density values measured in the dark conditions at 1.5 V *vs.* SCE were 1.5, 13.6 and 7.6 mA g^{-1} for ZnO, ZnO/CTAB and ZnO/F127, respectively. When the photoanodes were illuminated with 90 mW cm^{-2} the current density increased and at 1.5 V *vs.* SCE the measured values were 10.4, 27.0 and 20.0 mA g^{-1} for ZnO, ZnO/CTAB and ZnO/F127, respectively. Illumination of the photoanodes also induced a significant shift of the overpotential toward lower values; the most significant decrease in potential, from 1.296 to 0.248 V *vs.* SCE, was measured when ZnO/CTAB was used as the photoanode. Fig. 11(b) shows the typical chronoamperometric response of the ZnO photoanodes recorded in the on/off regime under illumination of 90 mW cm^{-2} at the potential of 1.5 V *vs.* SCE. As can be seen from Fig. 11(b), all microwave processed ZnO materials are slightly active in dark conditions. However, these materials become active when they absorb visible light; light energy knocks electrons from the valence band to the conduction band, generating photoexcitons.[87] The on/off ratio for the ZnO, ZnO/CTAB and ZnO/F127 photoanodes were found to be 5.9, 14 and 6.9, respectively. The ZnO/CTAB photoanode showed a higher photoresponse than ZnO and ZnO/F127 ones, which is 1.9 and 1.5-fold higher. The higher on/off ratio confirmed the profound effects of the optimal surface-to-bulk defect ratio in ZnO/CTAB by prolonging the electron–hole pair recombination time and faster carrier transport to the electrode.[88] These results are in accordance with LSV measurements. The stability of photocurrent signals is verified under repeated on/off regimes and under continual illumination confirming the resistivity of the of the point defects to photocorrosion and prolonged catalysts lifetime of the microwave processed ZnO materials. This confirmation of the point defects stability is more important knowing that V_O sites can be easily passivated by the adsorbed H_2O and CO_2 during photocatalytic reactions.[85,89] Besides, the activation energies needed for the photo-ionization of V_O to V_O^+ and V_O^{2+} are low, ~2.0 eV and ~2.3 eV, respectively.[89] The photo-ionized oxygen vacancies can be neutralized to V_O by a recombination process with the photogenerated electron or intrinsic electrons, eqn (12) and (13):[85]

$$V_O + h\nu \rightarrow V_O^+ + e^- \text{ or } V_O^{2+} + 2e^- (\text{Photo} - \text{activation}) \quad (12)$$

$$V_O^+ + e^- = V_O \text{ or } V_O^{2+} + 2e^- = V_O (\text{Recombination}) \quad (13)$$

To explain the effects of the surfactants, *i.e.* surface-to-bulk defects ratio on the photoresponse and charge transport phenomena,[90,91] Nyquist plots for the three ZnO photoanodes were recorded in dark and under illumination, at the potential of 1.5 V *vs.* SCE. The Nyquist plots display similar semicircles with different radii, Fig. 12(a); the radii were significantly reduced during illumination. The smallest semicircle was recorded for the ZnO/CTAB photoanode, which indicates that its resistance to the carrier transfer from the photoanode bulk to the surface was the smallest, *i.e.* the separation efficiency was the largest.[90] Even though one semicircle can be clearly observed in the Nyquist plots, two semicircles can be distinguished by enlarging the high frequency range: smaller one in the higher frequency region (1–100 kHz) and predominant one in the medium frequency region (0.1 Hz to 1 kHz). According to literature data, the higher frequency region semicircle is attributed to the charge transfers and recombination processes occurring at the electrode/electrolyte interface, while the medium frequency region semicircle is attributed to electrochemical processes occurring at the photoanode/redox electrolyte interface.[91] The diameters of the semicircles in the Nyquist plots signify the charge transfer kinetics at the electrode interface.[17] Therefore, to determine the diameter of the semicircles, it was necessary to fit the Nyquist plots by an equivalent circuit. For the given data-set (Nyquists plots), it is always possible to apply more than one equivalent circuit model that can fit the data and it is necessary to find an appropriate physics-based mathematical model for fitting. Among several tested models we choose to fit it with a circuit consisting of two parallel resistor (R) and constant phase elements (CPE) connected in a series plus one more R connected in a series, inset in Fig. 12(a); the parameters obtained by fitting of the Nyquists plots are listed in Table 5. The R_s is the series resistance of the electrochemical device the value of which represents the sum of the FTO substrate resistance, the resistance related to the ionic conductivity in the electrolyte and the external contact resistance. The R_s values obtained by fitting varied between 55 and 60 Ω; however, since R_s should be a constant independent of the photoanode, the values are not presented in Table 5. The CPE1 and R1 are attributed to the high-frequency arc describing the

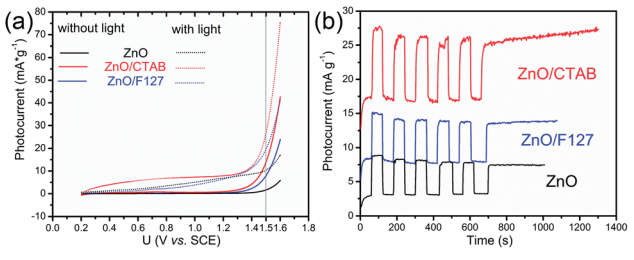

Fig. 11 (a) Linear sweep voltammograms of ZnO photoanodes in 0.1 M Na_2SO_4 solution at scan rate 20 mV s^{-1} in dark condition and under visible light illumination, and (b) chronoamperometric current density *vs.* time (J–t) response of the ZnO photoanodes measured at 1.5 V *vs.* SCE in dark condition and under visible light illumination.

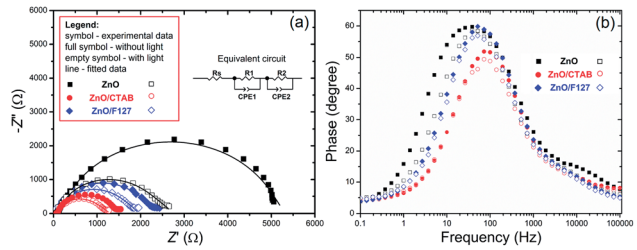

Fig. 12 (a) EIS of the ZnO photoanodes recorded in dark condition and under visible light illumination with the equivalent circuit model as an inset, and (b) Bode phase plots.

Table 5 Parameters obtained by fitting of EIS plots with the equivalent circuit presented in Fig. 12(a)

	Dark conditions				Light illumination			
Sample	R1 (Ω)	CPE1 (F)	R2 (Ω)	CPE2 (F)	R1 (Ω)	CPE1 (F)	R2 (Ω)	CPE2 (F)
ZnO	57.1	2.67×10^{-5}	5271	1.32×10^{-5}	40.9	2.24×10^{-5}	2454	1.49×10^{-5}
ZnO/CTAB	37.4	2.08×10^{-5}	1361	1.34×10^{-5}	33.7	2.34×10^{-5}	1119	1.94×10^{-5}
ZnO/F127	31.9	1.41×10^{-5}	2204	1.27×10^{-5}	30.4	1.75×10^{-5}	1754	1.52×10^{-5}

charge transfer in the bulk, while the CPE2 and R2 are attributed to the predominant arc, describing the charge transfer processes on the photoanode/electrolyte interface.[92,93] Generally, the charge transfer processes in the bulk are faster than the charge transfer processes on the interface of the photoanode/electrolyte.[94] The fitting of the Nyquist plots recorded in the dark conditions gives R2 values of 5271, 1361 and 2204 Ω cm^{-2} for ZnO, ZnO/CTAB and ZnO/F127, respectively. For the Nyquist plots recorded under illumination, the fitting shows reduced R2 values of 2454, 1119 and 1754 Ω cm^{-2}. Therefore, ZnO/CTAB shows the smallest resistance to the charge transfer processes on the photoanode/electrolyte interfaces; this result is in accordance with the highest photocurrent obtained by the LSV measurement, as well as with the photoresponse. The EIS results indicate that the ZnO/CTAB photoanode provides the most efficient charge transfer across the electrode/electrolyte interface, with a longer lifetime of photogenerated electron–hole pairs and reduced possibility of charge recombination.[95,96]

The charge separation dynamics of ZnO photoanodes is estimated according to the electron lifetime (τ_e) which can be calculated from the maximum peak frequency (f_{max}) in the mid-frequency region of the Bode plots (Fig. 12b) using eqn (14):[19]

$$\tau_e = 1(2\pi f_{max})^{-1} \quad (14)$$

The calculated electron lifetimes of ZnO, ZnO/CTAB and ZnO/F127 are 4.1, 2.2 and 3.1 ms, respectively. The shortest electron lifetime found for ZnO/CTAB suggests the fastest charge transfer of electrons across electrode/electrolyte interface in ZnO/CTAB as the photoanode.

The photoconversion efficiency values are calculated based on the *J–V* curves using eqn (15):[97]

$$\eta(\%) = \frac{J(1.23 - V_{applied})}{P_{in}} \quad (15)$$

where: J is the photocurrent (A g^{-1}), $V_{applied}$ is the applied potential *vs.* SCE, and P_{in} is the power of the incident light which is in this case 90 mW cm^{-2}. The photoconversion efficiency of the ZnO photoanodes as a function of applied potential is shown in Fig. 13; the ZnO/CTAB photoanode shows the largest photoconversion efficiency attaining 4.2% at 0.520 V *vs.* SCE which is, at the same potential, about 3.0 and 4.7-fold larger than that of ZnO and ZnO/F127, respectively. The ZnO photoanode reaches the maximal efficiency of 1.65% at 0.791 V *vs.* SCE while the ZnO/F127 photoanode achieves the maximal efficiency of 1.23% at 0.713 V *vs.* SCE.

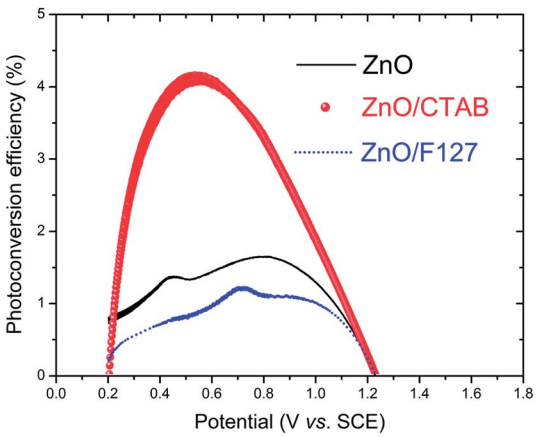

Fig. 13 Photoconversion efficiency of ZnO photoanodes as a function of applied potential.

4. Conclusions

We have established an eco-friendly, rapid and low-cost processing method for obtaining highly photo(electro) catalytically active ZnO particles. The proposed method, which uses a small amount of surfactants (CTAB and Pluronic F127), allows tuning of nano-crystallite polarity, particle texture, morphology, and surface-to-bulk defect ratio. In our study, the synergy of these properties resulted in enhanced optical and photo(electro) catalytic properties of ZnO particles. The best photo(electro) catalytic properties were exhibited by the ZnO/CTAB sample. After 2 hours under direct sunlight illumination, ZnO/CTAB photocatalysts efficiently (100%) decolorized 10 ppm MB dye water solution, with a decolorization halftime, $t_{1/2}$, of 26.42 min. ZnO/CTAB exhibited excellent properties as a photoanode. When the ZnO/CTAB photoanode was illuminated with 90 mW cm^{-2} the current density, measured at 1.5 V *vs.* SCE, reached 27.0 mA g^{-1}. Illumination of the ZnO/CTAB photoanode induced a significant shift of the overpotential toward lower values, namely from 1.296 to 0.248 V *vs.* SCE. Compared to ZnO and ZnO/F127, the ZnO/CTAB photoanode showed a higher photoresponse which was 1.9 and 1.5-fold higher. The ZnO/CTAB photoanode provides an efficient charge transfer across the electrode/electrolyte interface, with a longer lifetime of photogenerated electron–hole pairs and reduced possibility of charge recombination. The fastest charge transfer of electrons across the electrode/electrolyte interface acts with ZnO/CTAB as the photoanode. The photoconversion efficiency of ZnO/CTAB

was 4.2%. XRD, Raman, PL, and EIS analyses reveal that the optimal surface-to-bulk defect ratio is favorable for improvement of photo(electro)catalytic properties.

Conflicts of interest

There are no conflicts to declare.

Acknowledgements

This study was supported by the Ministry of Education, Science and Technological Development of the Republic of Serbia, Grant no III45004, and the bilateral cooperation program between the Republic of Serbia and the Republic of Slovenia "Nanostructured and mesoporous functional materials with enhanced solar light driven photocatalytic activity" for 2018–2019.

References

1 A. Fujishima and K. Honda, *Nature*, 1972, **238**(5358), 37–38.
2 S. Girish Kumar and K. S. R. Koteswara Rao, *RSC Adv.*, 2015, **5**, 3306–3351.
3 X. Chen, Y. Li, X. Pan, D. Cortie, X. Huang and Z. Yi, *Nat. Commun.*, 2016, **7**, 12273.
4 P. Kumar, R. Boukherroub and K. Shankar, *J. Mater. Chem. A*, 2018, **6**, 12876–12931.
5 S. Anantharaj, S. R. Ede, K. Sakthikumar, K. Karthick, S. Mishra and S. Kundu, *ACS Catal.*, 2016, **6**, 8069–8097.
6 S. Guo, X. Zhao, W. Zhang and W. Wang, *Mater. Sci. Eng., B*, 2018, **227**, 129–135.
7 K. Afroz, M. Moniruddin, N. Bakranov, S. Kudaibergenov and N. Nuraje, *J. Mater. Chem. A*, 2018, **6**, 21696–21718.
8 Y. Li, X. Zhang, S. Jiang, H. Dai, X. Sun and Y. Li, *Sol. Energy Mater. Sol. Cells*, 2015, **132**, 40–46.
9 S. Marković, A. Stanković, J. Dostanić, Lj. Veselinović, L. Mančić, S. D. Škapin, G. Dražić, I. Janković-Častvan and D. Uskoković, *RSC Adv.*, 2017, **7**, 42725–42737.
10 G. Liao, J. Chen, W. Zeng, C. Yu, C. Yi and Z. Xu, *J. Phys. Chem. C*, 2016, **120**, 25935–25944.
11 G. Liao, W. Zhao, Q. Li, Q. Pang and Z. Xu, *Chem. Lett.*, 2017, **46**, 1631–1634.
12 G. Liao, Q. Li, W. Zhao, Q. Pang, H. Gao and Z. Xu, *Appl. Catal., A*, 2018, **549**, 102–111.
13 A. A. Ismail and D. W. Bahnemann, *Sol. Energy Mater. Sol. Cells*, 2014, **128**, 85–101.
14 Z. Liu, C. Ma, Q. Cai, T. Hong, K. Guo and L. Yan, *Sol. Energy Mater. Sol. Cells*, 2017, **161**, 46–51.
15 C. Y. Toe, H. L. Tan, C. Boyer, A. Rawal, S. C. Thickett, J. Scott, R. Amala and Y. H. Ng, *J. Mater. Chem. A*, 2017, **5**, 4568–4575.
16 J. Abed, M. AlMheiri, F. Alexander, N. S. Rajput, J. Viegas and M. Jouiad, *Sol. Energy Mater. Sol. Cells*, 2018, **180**, 228–235.
17 R. Kant, S. Pathak and V. Dutta, *Sol. Energy Mater. Sol. Cells*, 2018, **178**, 38–45.
18 W. Zhang, W. Wang, H. Shi, Y. Liang, J. Fu and M. Zhu, *Sol. Energy Mater. Sol. Cells*, 2018, **180**, 25–33.
19 X. Zhang, Y.-Z. Zhou, D.-Y. Wu, X.-H. Liu, R. Zhang, H. Liu, C.-K. Dong, J. Yang, S. A. Kulinich and X.-W. Du, *J. Mater. Chem. A*, 2018, **6**, 9057–9063.
20 G. Liao, J. Fang, Q. Li, S. Li, Z. Xu and B. Fang, *Nanoscale*, 2019, **11**, 7062–7096.
21 W. Zhong, S. Shen, S. Feng, Z. Lin, Z. Wang and B. Fang, *CrystEngComm*, 2018, **20**, 7851–7856.
22 W. Zhong, W. Tu, S. Feng and A. Xu, *J. Alloys Compd.*, 2019, **772**, 669–674.
23 Y. Liu, S. Shen, J. Zhang, W. Zhong and X. Huang, *Appl. Surf. Sci.*, 2019, **478**, 762–769.
24 H. Zhu, D. Liu, D. Zou and J. Zhang, *J. Mater. Chem. A*, 2018, **6**, 6130–6154.
25 X. Wang, K. Maeda, A. Thomas, K. Takanabe, G. Xin, J. M. Carlsson, K. Domen and M. Antonietti, *Nat. Mater.*, 2009, **8**, 76–80.
26 G. Liao, Y. Gong, L. Zhang, H. Gao, G. Yang and B. Fang, *Energy Environ. Sci.*, 2019, DOI: 10.1039/c9ee00717b.
27 X. Chen, L. Liu, P. Y. Yu and S. S. Mao, *Science*, 2011, **331**, 746–750.
28 W. Li, R. Liang, A. Hu, Z. Huanga and Y. N. Zhou, *RSC Adv.*, 2014, **4**, 36959–36966.
29 T. Xia, P. Wallenmeyer, A. Anderson, J. Murowchick, L. Liu and X. Chen, *RSC Adv.*, 2014, **4**, 41654–41658.
30 S. Marković, V. Rajić, A. Stanković, Lj. Veselinović, J. Belošević-Čavor, K. Batalović, N. Abazović, S. D. Škapin and D. Uskoković, *Sol. Energy*, 2016, **127**, 124–135.
31 A. Janotti and C. G. Van de Walle, *Phys. Rev. B: Condens. Matter Mater. Phys.*, 2007, **76**, 165202–165222.
32 J. Highfield, *Molecules*, 2015, **20**, 6739–6793.
33 M. Kong, Y. Li, X. Chen, T. Tian, P. Fang, F. Zheng and X. Zhao, *J. Am. Chem. Soc.*, 2011, **133**, 16414–16417.
34 H. Silva, C. Mateos-Pedrero, C. Magen, D. A. Pacheco Tanaka and A. Mendes, *RSC Adv.*, 2014, **4**, 31166–31176.
35 Q. Liu, Z. Sun, Y. Dou, J. H. Kim and S. X. Dou, *J. Mater. Chem. A*, 2015, **3**, 11688–11699.
36 P. Bai, P. Wu, Z. Yan, J. Zhou and X. S. Zhao, *J. Phys. Chem. C*, 2007, **111**, 9729–9733.
37 R. Garvey, LSUCRIPC, Least squares unit-cell refinement with indexing on the personal computer, *Powder Diffr.*, 1986, **1**, 114–118.
38 H. P. Klug and L. E. Alexander, *X-ray diffraction procedures for polycrystalline and amorphous materials*, Wiley, New York, 4th edn, 1954.
39 S. K. Pardeshi and A. B. Patil, *J. Mol. Catal. A: Chem.*, 2009, **308**, 32–40.
40 F. Rouquerol, J. Rouquerol and K. Sing, *Adsorption by powders and porous solids*, Academic Press, London, 1999.
41 E. P. Barrett, L. G. Joyner and P. P. Halenda, *J. Am. Chem. Soc.*, 1951, **73**, 373–380.
42 G. R. Li, T. Hu, G. L. Pan, T. Y. Yan, X. P. Gao and H. Y. Zhu, *J. Phys. Chem. C*, 2008, **112**, 11859–11864.
43 A. Mclaren, T. Valdes-Solis, G. Li and S. C. Tsang, *J. Am. Chem. Soc.*, 2009, **131**, 12540–12541.
44 Y.-X. Wang, J. Sun, X. Y. Fan and X. Yu, *Ceram. Int.*, 2011, **37**, 3431–3436.

45 I. Stambolova, V. Blaskov, D. Stoyanova, I. Avramova, L. Dimitrov, K. Milenova, K. Balashev, S. Simeonova, A. Tzonev, L. Aleksandrov and A. Eliyas, *Bull. Mater. Sci.*, 2017, **40**, 483–492.
46 Y. Wang, X. Li, G. Lu, G. Chen and Y. Chen, *Mater. Lett.*, 2008, **62**, 2359–2362.
47 R. Yi, N. Zhang, H. Zhou, R. Shi, G. Qiu and X. Liu, *Mater. Sci. Eng., B*, 2008, **153**, 25–30.
48 A. Stanković, Z. Stojanović, Lj. Veselinović, S. D. Škapin, I. Bračko, S. Marković and D. Uskoković, *Mater. Sci. Eng., B*, 2012, **177**, 1038–1045.
49 A. Stanković, S. Dimitrijević and D. Uskoković, *Colloids Surf., B*, 2013, **102**, 21–28.
50 A. Sadollahkhani, I. Kazeminezhad, J. Lu, O. Nur, L. Hultman and M. Willander, *RSC Adv.*, 2014, **4**, 36940–36950.
51 R. N. Moussawi and D. Patra, *RSC Adv.*, 2016, **6**, 17256–17268.
52 I. M. El-Nahhal, J. K. Salem, N. S. Tabasi, R. Hempelmann and F. S. Kodeh, *Chem. Phys. Lett.*, 2018, **691**, 211–218.
53 R. Cuscó, E. Alarcón-Lladó, J. Ibáñez, L. Artús, J. Jiménez, B. Wang and M. J. Callahan, *Phys. Rev. B: Condens. Matter Mater. Phys.*, 2007, **75**, 165202.
54 K. F. Lin, H. M. Cheng, H. C. Hsu and W. F. Hsieh, *Appl. Phys. Lett.*, 2006, **88**, 263117.
55 R. Sánchez Zeferino, M. Barboza Flovers and U. Pal, *J. Appl. Phys.*, 2011, **109**, 014308.
56 Y. Li, G. Dai, C. Zhou, Q. Zhang, Q. Wan, L. Fu, J. Zhang, R. C. Cao, A. Pan, Y. Zhang and B. Zou, *Nano Res.*, 2010, **3**, 326–338.
57 R. Jothilakshmi, V. Ramakrishnan, R. Thangavel, J. Kumar, A. Saruac and M. Kuball, *J. Raman Spectrosc.*, 2009, **40**, 556–561.
58 M. Šćepanović, M. Grujić-Brojčin, K. Vojisavljević, S. Bernik and T. Srećković, *J. Raman Spectrosc.*, 2010, **41**, 914–921.
59 H. J. Fan, R. Scholz, F. M. Kolb, M. Zacharias, U. Gösele, F. Heyroth, C. Eisenschmidt, T. Hempel and J. Christen, *Appl. Phys. A: Mater. Sci. Process.*, 2004, **79**, 1895–1900.
60 S. Sahoo, G. L. Sharma and R. S. Katiyar, *J. Raman Spectrosc.*, 2012, **43**, 72–75.
61 X. Sui, C. Shao and Y. Liu, *Polymer*, 2007, **48**, 1459–1463.
62 C.-K. Wu, K. Sivashanmugan, T.-F. Guo and T.-C. Wen, *Materials*, 2018, **11**, 378.
63 S. Liu, C. Li, J. Yu and Q. Xiang, *CrystEngComm*, 2011, **13**, 2533–2541.
64 N. S. Han, H. S. Shim, J. H. Seo, S. Y. Kim, S. M. Park and J. K. Song, *J. Appl. Phys.*, 2010, **107**, 084306.
65 S. B. Rana, *J. Mater. Sci.: Mater. Electron.*, 2017, **28**, 13787–13796.
66 H. Zeng, G. Duan, Y. Li, S. Yang, X. Xu and W. Cai, *Adv. Funct. Mater.*, 2010, **20**, 561–572.
67 J.-H. Lin, R. A. Patil, R. S. Devan, Z.-A. Liu, Y.-P. Wang, C.-H. Ho, Y. Liou and Y.-R. Ma, *Sci. Rep.*, 2014, **4**, 6967.
68 B. Jin and D. Wang, *J. Lumin.*, 2012, **132**, 1879–1884.
69 C. H. Ahn, Y. Y. Kim, D. C. Kim, S. K. Mohanta and H. K. Cho, *J. Appl. Phys.*, 2009, **105**, 013502.
70 C. H. Ahn, Y. Y. Kim, D. C. Kim, S. K. Mohanta and H. K. Cho, *J. Appl. Phys.*, 2009, **105**, 089902.
71 B. Lin, Z. Fu and Y. Jia, *Appl. Phys. Lett.*, 2001, **79**, 943–945.
72 H. Zeng, Z. Li, W. Cai and P. Liu, *J. Appl. Phys.*, 2007, **102**, 104307.
73 J. R. Sadaf, M. Q. Israr, O. Nur, M. Willander, Y. Ding and Z. L. Wang, *Nanoscale Res. Lett.*, 2011, **6**, 513.
74 Y. Hong, C. Tian, B. Jiang, A. Wu, Q. Zhang, G. Tian and H. Fu, *J. Mater. Chem. A*, 2013, **1**, 5700–5708.
75 Md. Elias, Md. Khairul Amin, S. H. Firoz, Md. Asjad Hossain, S. Akter, Md. Awlad Hossain, Md. Nizam Uddin and I. Ahmed Siddiquey, *Ceram. Int.*, 2017, **43**, 84–91.
76 M. Irani, T. Mohammadi and S. Mohebbi, *J. Mex. Chem. Soc.*, 2016, **60**, 218–225.
77 S.-Y. Pung, W.-P. Lee and A. Aziz, *Int. J. Inorg. Chem.*, 2012, 608183.
78 C. A. Aggelopoulos, M. Dimitropoulos, A. Govatsi, L. Sygellou, C. D. Tsakiroglou and S. N. Yannopoulos, *Appl. Catal., B*, 2017, **205**, 292–301.
79 Q. Xie, J. Li, Q. Tian and R. Shi, *J. Mater. Chem.*, 2012, **22**, 13541–13547.
80 H. Vahdat Vasei, S. M. Masoudpanah, M. Adeli and M. R. Aboutalebi, *Ceram. Int.*, 2018, **44**, 7741–7745.
81 A. Ajmal, I. Majeed, R. Naseem Malik, H. Idriss and M. Amtiaz Nadeem, *RSC Adv.*, 2014, **4**, 37003–37026.
82 R. S. Dariani, A. Esmaeili, A. Mortezaali and S. Dehghanpour, *Optik*, 2016, **127**, 7143–7154.
83 X. Zhang, J. Qin, Y. Xue, P. Yu, B. Zhang, L. Wang and R. Liu, *Sci. Rep.*, 2014, **4**, 4596.
84 H. Zhao, F. Pan and Y. Li, *J. Materiomics*, 2017, **3**, 17–32.
85 L. Tsui and G. Zangari, *J. Electrochem. Soc.*, 2014, **161**, 3066–3077.
86 J. Yan, G. Wu, N. Guan, L. Li, Z. Li and X. Cao, *Phys. Chem. Chem. Phys.*, 2013, **15**, 10978–10988.
87 I. Khan, A. A. M. Ibrahim, M. Sohail and A. Qurashi, *Ultrason. Sonochem.*, 2017, **37**, 669–675.
88 T. Majumder, J. J. L. Hmar, S. Dhar and S. P. Mondal, *Chem. Phys.*, 2017, **490**, 1–6.
89 Z. Yang, T. Meng, Q. Zhang and H.-P. D. Shieh, *IEEE Electron Device Lett.*, 2016, **37**, 437–440.
90 Z. Zhou, S. Wu, L. Qin, L. Li, L. Li and X. Li, *J. Mater. Chem. A*, 2018, **6**, 15593–15602.
91 M. S. Ansari, A. Banik, A. Kalita, P. K. Iyer and M. Qureshi, *J. Mater. Chem. A*, 2018, **6**, 15868–15887.
92 T. Majumder and S. P. Mondal, *J. Electroanal. Chem.*, 2016, **769**, 48–52.
93 S. Guo, S. Wang, N. Wu, J. Liu, Y. Ni and W. Liu, *RSC Adv.*, 2015, **5**, 103767–103775.
94 T. Lopes, L. Andrade, F. L. Formal, M. Gratzel, K. Sivula and A. Mendes, *Phys. Chem. Chem. Phys.*, 2014, **16**, 16515–16523.
95 F. Rasouli, A. Rouhollahi and F. Ghahramanifard, *Mater. Sci. Semicond. Process.*, 2019, **93**, 371–378.
96 Y. C. Weng and K. T. Hsiao, *Int. J. Hydrogen Energy*, 2015, **40**, 3238–3248.
97 M. G. Walter, E. L. Warren, J. R. McKone, S. W. Boettcher, Q. Mi, E. A. Santori and N. S. Lewis, *Chem. Rev.*, 2010, **110**, 6446–6473.